Dirac-electron-mediated magnetic proximity effect in topological insulator/magnetic insulator heterostructures

Citation: Li, Mingda et al. "Dirac-Electron-Mediated Magnetic Proximity Effect in Topological Insulator/magnetic Insulator Heterostructures." Physical Review B 96, 20 (November 2017): 201301(R) © 2017 American Physical Society

As Published: http://dx.doi.org/10.1103/PHYSREVB.96.201301

Publisher: American Physical Society (APS)

Persistent URL: http://hdl.handle.net/1721.1/117658

Version: Final published version: final published article, as it appeared in a journal, conference proceedings, or other formally published context

PHYSICAL REVIEW B **96**, 201301(R) (2017)

Dirac-electron-mediated magnetic proximity effect in topological insulator/magnetic insulator heterostructures

Mingda Li,[1,2,*] Qichen Song,[1] Weiwei Zhao,[3] Joseph A. Garlow,[4] Te-Huan Liu,[1] Lijun Wu,[4] Yimei Zhu,[4] Jagadeesh S. Moodera,[5,6] Moses H. W. Chan,[3] Gang Chen,[1,*] and Cui-Zu Chang[3,5,*]

[1]*Department of Mechanical Engineering, MIT, Cambridge, Massachusetts 02139, USA*

[2]*Department of Nuclear Science and Engineering, MIT, Cambridge, Massachusetts 02139, USA*

[3]*Department of Physics, The Pennsylvania State University, University Park, Pennsylvania16802, USA*

[4]*Condensed Matter Physics and Materials Science Department, Brookhaven National Lab, Upton, New York 11973, USA*

[5]*Francis Bitter Magnet Lab, MIT, Cambridge, Massachusetts 02139, USA*

[6]*Department of Physics, MIT, Cambridge, Massachusetts 02139, USA*

(Received 2 June 2017; published 1 November 2017)

The possible realization of dissipationless chiral edge current in a topological insulator/magnetic insulator heterostructure is based on the condition that the magnetic proximity exchange coupling at the interface is dominated by the Dirac surface states of the topological insulator. Here we report a polarized neutron reflectometry observation of Dirac-electron-mediated magnetic proximity effect in a bulk-insulating topological insulator $(Bi_{0.2}Sb_{0.8})_2Te_3$/magnetic insulator EuS heterostructure. We are able to maximize the proximity-induced magnetism by applying an electrical back gate to tune the Fermi level of topological insulator to be close to the Dirac point. A phenomenological model based on diamagnetic screening is developed to explain the suppressed proximity-induced magnetism at high carrier density. Our work paves the way to utilize the magnetic proximity effect at the topological insulator/magnetic insulator heterointerface for low-power spintronic applications.

DOI: 10.1103/PhysRevB.96.201301

Magnetic proximity effect (MPE) in a topological insulator (TI)/magnetic insulator (MI) heterostructure induces magnetization to the TI's electronic states driven by means of magnetic exchange coupling from the MI layer [1–14]. As long as the MPE-induced magnetic order is realized through the Dirac electrons, this effect is expected to have applications in low-energy-consumption electronic and spintronic devices [1,2,15–17]. One prominent application is the quantum anomalous Hall effect (QAHE), where dissipationless chiral edge current can be harbored without external magnetic field [18–24]. Comparing with the other approach to magnetize the Dirac surface state (DSS) by doping the TI with transitional-metal ions [20,21,25–29], the MPE approach has the advantage that it can result in a uniform magnetization over the entire TI layer without creating any impurity sites nor destroying the nontrivial band structure [2,8,14,30]. While the QAHE to date has been realized in Cr- and V- doped TI systems [18–20,22,23,27], no QAHE has been hitherto demonstrated in a MPE-induced ferromagnetism system in spite of extensive studies. This brings up a few fundamental questions: Is the MPE actually happening to the DSS of TI? If so, what is the nature of the MPE-induced ferromagnetic order in DSS? For the first question, MPE in principle can happen to any electronic states of TI, including bulk states [31]. As to the second question, if, for instance, the MPE is realized through coupling with free carriers of the TI, the MPE will be enhanced by increasing the carrier density, hence hampering QAHE due to its carrier-free requirement [21]. Therefore, an experimental study on the correlation between the carrier density and the magnitude of MPE in TI will show whether the MPE through a MI is a viable route to realize QAHE.

Recently, the contribution of the bulk n-type carriers to MPE in a highly n-doped TI Bi_2Se_3/MI EuS heterostructure was studied through polarized neutron reflectometry (PNR) [9]. In this paper, by further equipping the PNR spectrometer with additional electrical transport capability and bottom-gate voltage (V_g), we are able to resolve the DSS's contribution to the proximity-induced magnetism at the interface between TI $(Bi_{0.2}Sb_{0.8})_2Te_3$ and MI EuS. Specifically, we found the maximum proximity-induced magnetism is realized when the Fermi level is close to the Dirac point.

The PNR experiments were carried out at beamline NG-D at the NIST Center for Neutron Research, at fixed temperature $T = 5$ K. PNR is a powerful technique for measuring the real-space magnetic structure of thin films [32]. The experimental setup is illustrated in Fig. 1(b), where the incident spin-polarized neutron beams are reflected by the MI/TI heterostructure (red and blue spheres), while the spin nonflip reflectivity signals from spin-up and spin-down components, $R_\uparrow$ and $R_\downarrow$, are collected alternatively. The PNR is integrated with a custom-built sample holder [Fig. 1(b) and see Supplemental Material [33] for the image of the experimental setup, the x-ray diffraction (XRD), the interpretation of spin asymmetry, fitting scheme, and fixed-scattering length density (SLD) fitting for the image of the experimental setup], which allows *in situ* gate-dependent two-terminal longitudinal transport measurement while performing the PNR measurements. A $\mu_0 H = 0.7$ T guide field is exerted at all times to prevent possible neutron depolarization. Figure 1(a) is a schematic of the EuS/$(Bi_{0.2}Sb_{0.8})_2Te_3$ heterostructure. Both perpendicular magnetization, which causes the surface state band-gap opening [21], and the in-plane magnetization, which results in the shift of the Dirac cone [24], are capable of

*Authors to whom correspondence should be addressed: mingda@mit.edu; gchen2@mit.edu; cxc955@psu.edu

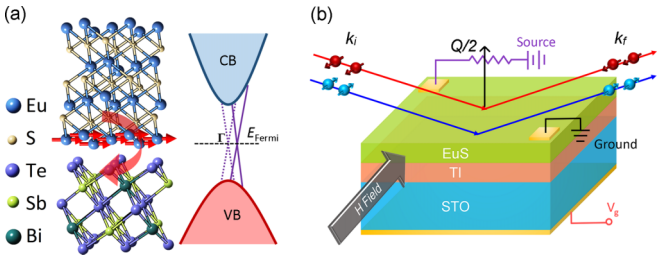

FIG. 1. (a) Atomic configuration (left) and schematic band structure (right) at the MI/TI interface. When the ferromagnetic Eu ions magnetize the surface state of the TI (red arrow in left figure), the original Dirac cone (purple dotted lines) is shifted away from Γ point (purple solid lines) through exchange coupling, causing MPE. (b) Schematics of the gate-dependent neutron reflectometry system, where the incident neutron momentum, reflected neutron momentum, and the momentum change are denoted as k_i, k_f, and Q ($Q \equiv k_i - k_f$), respectively. The two neutron spins switched by a spin flipper shine onto the sample alternatively. See Sec. I of the Supplemental Material [33] for an image of the setup.

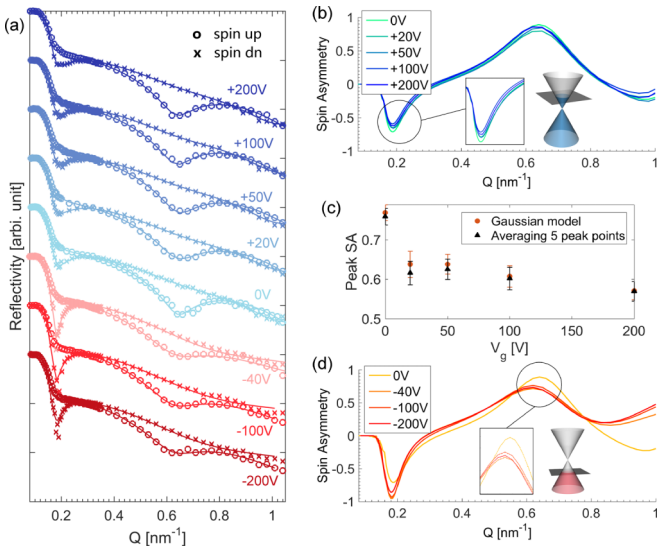

FIG. 2. (a) Experimental measured (o and x dots) and theoretically refined (solid lines) PNR reflectivity (in log scale) vs Q of both spin components $R_\uparrow$ and $R_\downarrow$, at various back-gate voltages $V_g = 0, +20, +50, +100, +200, -200, -100$, and -40 V (based on the measuring sequence). Q is the magnitude of the neutron momentum change, where at low Q, $R_\uparrow = R_\downarrow = 1$. Each reflectivity curve is vertically shifted by 10^2 for clarity. (b), (d) Spin asymmetry at positive and negative V_gs, respectively. Even before any refinement, a higher spin-asymmetry peak can be seen at low V_g, indicating a greater change of local magnetic structure at small V_g, as shown in (c).

inducing QAHE. In the present setup, we focus on the in-plane magnetization, yet there might still be a canting effect which allows the spin rotation toward the perpendicular direction [9]. The reason for choosing a Eu-based element as proximity layer is its extremely high neutron absorption cross section [$\sigma_A(Eu) = 4530$ barn], which helps to identify the location of the proximity layer and has been implemented in a few recent studies [8,9]. Moreover, an ambipolar behavior of MPE is revealed, that for both n- and p-doped TI, the MPE is reduced when the carrier density is increased. This strongly suggests that the MPE in a TI/MI heterostructure is not originated from the free carriers and hence enables the MPE-based QAHE. The reduced proximity-induced magnetism at increased carrier density can be understood as a diamagnetic screening effect. We have developed a phenomenological model to explain this effect qualitatively. Our study sheds light on further exploring the direction of MPE toward next-generation dissipationless electronic and spintronic applications.

Since the purpose of this measurement is to detect the MPE's possible variation, which can be considered as a second-order effect if the ferromagnetism in MI layer is zeroth order and the induced MPE is a first-order effect, the sample quality becomes essential. High-quality MI 5-nm EuS/4 quintuple layers (QLs) intrinsic TI $(Bi_{0.2}Sb_{0.8})_2Te_3$ heterostructure is grown by molecular-beam epitaxy under a base vacuum $\sim 5 \times 10^{-10}$ Torr. The Bi:Sb ratio is carefully optimized to locate the Fermi level close to the Dirac point based on the method reported in Ref. [34]. The 4QL TI thickness is chosen to make sure no hybridization gap is formed on the surface states and to facilitate the bias-gate voltage tunability due to the low bulk-carrier concentration [35]. The TI thin film is grown on top of heat-treated 0.5-mm-thick $SrTiO_3$ (STO) (111) substrate for back-gating purpose. The high sample quality is checked from both XRD (see Sec. I of the Supplemental Material for the XRD [33]) and transmission electron microscopy (TEM) [Fig. 3(d)], where high-quality epitaxial growth is realized with sharp MI/TI interface.

The measured reflectivity curves at various V_g are plotted in Fig. 2(a), which are further refined by using the GENX program to extract the SLD profiles [36]. The "Best-1-Bin" algorithm has been implemented during the differential evolution refinement process, indicating a likelihood to achieve global optimization within a reasonable parameter range [37]. In fact, even prior to seeing the refined SLD, we could already tell the effect of voltage through raw data of spin asymmetry (SA), defined as $SA \equiv (R_\uparrow - R_\downarrow)/(R_\uparrow + R_\downarrow)$: at low V_g near the Dirac point (0 and +20 V) the peak SA at 0 V is higher and reduced at higher voltage, indicating a tunability of proximity through V_g [Figs. 2(b) and 2(c) and Sec. II of the Supplemental Material [33] for the interpretation of spin asymmetry]. The $V_g < 0$ part is not compared directly with the $V_g > 0$ part due to the sample heating and recooling between the measurements, to eliminate the STO memory effect when switching the V_g polarity, but the gate-voltage-dependent SA can still be seen clearly from Fig. 2(d) and the inset.

Upon fitting, the fitted curves [solid lines in Fig. 2(a)] show excellent agreement with the experiment data (filled points), with logarithmic figure of merit $<5 \times 10^{-2}$. To eliminate any hysteresis effect caused by the ferroelectricity of STO [38], the whole sample was warmed up to room temperature and cooled back down under high vacuum during the polarity change from +200 to −200 V. For this reason, a very small thickness and density variation is allowed in the refinement process to obtain better fitting quality (see Sec. III of the Supplemental Material [33] for fitting scheme). A global fitting of all spectra simultaneously with strictly fixed thickness and SLD

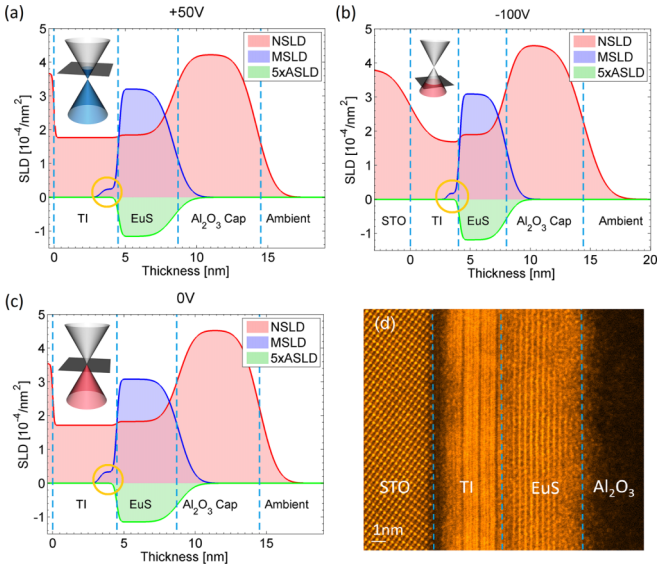

FIG. 3. (a)–(c) The SLD profiles at +50, +0, and −100 V, respectively. The NSLD contains the information of sample thickness and interfacial roughness, which agrees well with the TEM result in (d). From the MSLD, we can see that the magnetic proximity effect (yellow circled region) can be tuned through V_g, and is reduced for both n- and p- type doping. The ALSD signal solely comes from the Eu ions; hence, the lack of ASLD ~ 4 nm in the TI side indicates that the proximity-induced magnetism is not coming from the interdiffused Eu ions, which is further confirmed from the sharp TI/EuS interface in the TEM image. On the other hand, there are diffused Eu ions to the Al_2O_3 cap, which can be seen from both ASLD ~ 9 nm at rough interface of EuS/Al_2O_3 from the TEM.

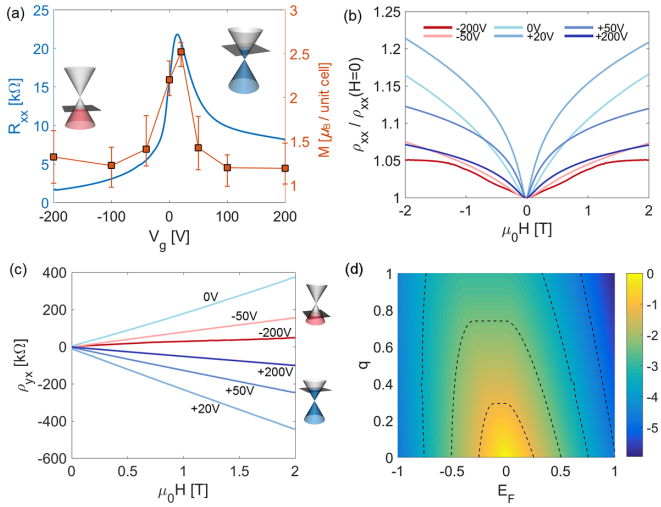

FIG. 4. (a) Sheet longitudinal resistance R_{xx} of the MI/TI heterostructure (blue curve) vs the proximity-induced magnetization M (orange dots), as a function of gate voltage V_g. The proximity-induced magnetism shows a peak near the Dirac point, where the R_{xx} also shows a peak. (b) Normalized longitudinal magnetoresistance $R_{xx}(H)$, from which a typical WAL behavior is seen in almost all bias voltages. (c) Hall resistance $R_{yx}(H)$ as a function of V_g. From the sign we can tell that at $V_g = 0$ V it is hole-doped ($R_{yx} > 0$), while at $V_g = 20$ V it is electron-doped ($R_{yx} < 0$). (d) Computed susceptibility χ as a function of Fermi level E_F and wave number q. A diamagnetic effect $\chi < 0$ is shown on both sides away from the Fermi level.

is performed independently using the REFL1D package [39], showing an identical qualitative trend that the proximity magnetism is higher at low gate voltage (see Sec. IV of the Supplemental Material [33] for fixed-SLD fitting).

The refined SLD profiles from the fitted reflectivity curves at a few representative V_g are plotted in Fig. 3. The resulting nuclear scattering length density (NSLD) agrees well with the expected cross-section calculation that the STO substrate gives $\sim 3.6 \times 10^{-4}$ nm^{-2}, TI layer $\sim 1.8 \times 10^{-4}$ nm^{-2}, EuS $\sim 1.9 \times 10^{-4}$ nm^{-2}, and amorphous Al_2O_3 capping layer $\sim 4 \times 10^{-4}$ nm^{-2}. From the magnetic scattering length density (MSLD), it can be seen clearly that at $V_g = +20$ V the proximity MSLD is increased to $2.5\mu_B$/unit cell, comparing with $\sim 1.2\mu_B$/unit cell at $V_g = +200$ V, which is comparable with a previous report in Ref. [8], where TI Sb_2Te_3 was used. The absorption scattering length density (ASLD) indicates the region of neutron absorption; in this system, the ASLD is solely coming from Eu atoms. The warming and cooling of the sample between $V_g > 0$ measurements and $V_g < 0$ measurements causes some change of STO/TI interfacial roughness [Fig. 3(a) vs Fig. 3(b)], making the fixed-SLD analysis valid for $V_g > 0$ only (see Sec. III of the Supplemental Material [33] for fitting scheme). Despite that two independent PNR refinement strategies and SA from raw data point to the same conclusion of peak proximity, we do not intend to fully exclude other possible SLD configurations due to the nuance effect caused by electric field.

At this stage, the effect of carrier density tuned through a V_g to the proximity-induced magnetism becomes clear. The MPE strength as a function of V_g is plotted in Fig. 4(a), together with the sheet longitudinal resistance R_{xx}. It can be seen clearly that the MPE shows a peak at $V_g \approx 0$ V, which coincides with the behavior of the R_{xx}, indicating that the highest MPE is realized near the Dirac point. Moreover, a finite carrier density–both n- or p- type–could reduce the MPE to the normal value as reported in Ref. [8]. On the other hand, the *ex situ* magnetoresistance (MR) is performed as well. For longitudinal MR measurement [Fig. 4(b)], a typical weak antilocalization (WAL) behavior is revealed at almost all voltages [40,41]. In the weak H regime, the MR shows a steeper increase when the Fermi level is closer to the Dirac point. This behavior is consistent with a previous report [42]. Besides, the Hall measurements are also performed [Fig. 4(c)], from which we could verify the carrier type and estimate the carrier density [43]. The lowest carrier density $n_{2D} = -2.8 \times 10^{12}$ cm^{-2} is located at $V_g = +20$ V. Since the carrier densities at $V_g = -200, -50, +50$, and $+200$ V are $n_{2D} = 2.64 \times 10^{13}$ cm^{-2}, 8.0×10^{12}cm^{-2}, -5.0×10^{12} cm^{-2}, and -2.75×10^{13} cm^{-2}, respectively, while the maximum Dirac electron carrier density accommodated in the spin-polarized Dirac cone of a TI gives $\sim 1.6 \times 10^{12}$ cm^{-2} (assuming $E_{gap} = 0.3$ eV and $v_F = 5 \times 10^5$m/s), we can see that the Fermi level is already tuned from the bulk valence band to the bulk conduction band even at low V_g. This is consistent with the report in Ref. [44] that the critical carrier density of the Dirac cone is $\sim 5.0 \times 10^{12}$ cm^{-2}, and is useful to simplify the theory discussed below. In addition, we

notice that the peak of MPE ($V_g \sim +25$ V by fitting) and the peak of R_{xx} ($V_g = +20$ V) have a slight mismatch, indicating that the transport and neutron scattering may have slightly different origins of the contributing carriers. One possible explanation is that the transport may have contributions from both bottom TI/STO interface and top TI/MI interface while the spatially resolved neutron is only sensitive to the top TI/MI interface. Even so, we believe the transport and neutron results are directly comparable, since the gating is strong enough to tune the Fermi level of the top surface due to the high dielectric constant of TI materials (∼100) [20,27,45].

At this point, one may wonder whether MPE is caused by Dirac electrons or if they merely have coincidental correlation. To further understand the implication in Fig. 4(a), we developed a simple phenomenological model to account for this ambipolar behavior from a perspective of magnetic susceptibility. It is well known that the bulk electronic bands of TI away from the Dirac point have a diamagnetic nature due to large orbital diamagnetism [31], where the total magnetic susceptibility χ_{tot} under the long-wavelength limit satisfies $\chi_{\text{tot}}(q \to 0) \sim -\frac{1}{3}\chi_s^B(q \to 0) < 0$, in which χ_s^B denotes the spin susceptibility for bulk bands. On the other hand, the DSS has a paramagnetic nature due to its small effective mass $\chi_{\text{tot}}(q \to 0) \sim +\frac{2}{3}\chi_s^D(q \to 0) > 0$, where χ_s^D denotes the spin susceptibility for DSS [31]. This indicates that whenever the Fermi level is near the Dirac point (lower carrier density n_{2D}), the total susceptibility is enhanced through the paramagnetic effect of DSS. On the other hand, when the Fermi level is shifted away from the Dirac point (high V_g), the diamagnetism starts to dominate and screens the proximity induced magnetism. Assuming a conduction-band minimum E_c and valence-band maximum E_v, the total susceptibility χ_{tot} as a function of Fermi level E_F can thus be written as a phenomenological piecewise function:

$$\chi_{\text{tot}}(E_F) \approx -\frac{1}{3}\chi_s^B(E_F)[\theta(E_F - E_c) + \theta(E_v - E_F)] + \frac{2}{3}\chi_s^D(E_F)[\theta(E_F - E_v) - \theta(E_F - E_c)], \quad (1)$$

where $\theta(x)$ is the Heaviside step function. The spin susceptibility χ_s can be written as [31]

$$\chi_s^{B,D}(\mathbf{q}) = \frac{\mu_B^2}{4\pi^3} \sum_{\substack{m,\text{occ} \\ n,\text{empty}}} \int d^3\mathbf{k} \frac{f_0\left(E_{n,\mathbf{k}}^{B,D}\right) - f_0\left(E_{m,\mathbf{k}+\mathbf{q}}^{B,D}\right)}{E_{m,\mathbf{k}+\mathbf{q}}^{B,D} - E_{n,\mathbf{k}}^{B,D} + i\delta}, \quad (2)$$

where $E_{n,\mathbf{k}}^{B,D}$ are the eigenvalues for the corresponding surface or bulk Hamiltonian; f_0 is the Fermi-Dirac distribution function. Here, by plugging the material-dependent eigenvalues [46] into Eq. (2), the susceptibility can be computed accordingly. For the particular EuS/$(Bi_{0.2}Sb_{0.8})_2Te_3$ system, due to the lack of the corresponding effective Hamiltonian, here only a qualitative picture is provided, which is sufficient to demonstrate whether carrier density can cause a unipolar (χ changes monotonically with E_F) or a ambipolar effect [$\chi(E_F = 0)$ is a local minimum or maximum]. Since the bias voltage is shown to be effective enough to tune E_F into bulk bands even at low V_g, assuming $E_v \approx E_c$ (small paramagnetic region) and neglecting all anisotropy, which allows a much simpler dispersion relation $E_{m,\mathbf{k}+\mathbf{q}} \sim E_{m,k+q} = \sqrt{k^2 + q^2}$ (the resulting trend does not depend on the particular form of dispersion), an ambipolar effect is revealed [Fig. 4(d)] that when E_F is away from the Dirac point, the diamagnetic screening gets stronger for both n- and p-type doping, hence reducing the MPE. This agrees with our experimental results in Fig. 4(a). At even higher E_F, the screening effect is saturated, since besides screening, other electronic states could directly contribute to the proximity-induced magnetism [31].

In summary, we showed the Dirac-electron-mediated MPE at the interface of a MI/TI heterostructure by means of gate-dependent PNR measurements. The tunability of the MPE enables future theoretical studies to utilize MPE to manipulate the interfacial spin texture in TI [47–49]. The maximum MPE, in particular, is realized when the Fermi level is approaching the Dirac point where carrier density is minimized. Since the realization of in-plane magnetization-induced QAHE requires both that the Fermi level is near the Dirac point together with the strong MPE, our study proves that the MPE is favored at low carrier concentration, which opens up the possibility for realizing in-plane magnetization-induced QAHE [24] at MI/TI heterostructure.

M.L., Q.S., and G.C. would like to acknowledge support by S^3TEC, an Energy Frontier Research Center funded by US Department of Energy (DOE), Office of Basic Energy Sciences (BES) under Award No. DE-SC0001299/DE-FG02-09ER46577 and DARPA MATRIX Program Contract No. HR0011-16-2-0041. M.L. and C.Z.C thank A. Grutter and B. Kirby for the helpful discussion. Y.Z. and L.W. acknowledge the support from DOE-BES / Materials Science and Engineering (MSE) division under Contract No. DE-AC02-98CH10886. J.S.M. acknowledges the support from NSF Grant No. DMR-1207469, ONR Grant No. N00014-16-1-2657, and the STC Center for Integrated Quantum Materials under NSF Grant No. DMR-1231319. C.Z.C would like to acknowledge support from the startup grant provided by Penn State University.

M.L. and Q.S. contributed equally to this work.

[1] I. Vobornik, U. Manju, J. Fujii, F. Borgatti, P. Torelli, D. Krizmancic, Y. S. Hor, R. J. Cava, and G. Panaccione, Nano Lett. **11**, 4079 (2011).

[2] M. Lang *et al.*, Nano Lett. **14**, 3459 (2014).

[3] P. Wei, F. Katmis, B. A. Assaf, H. Steinberg, P. Jarillo-Herrero, D. Heiman, and J. S. Moodera, Phys. Rev. Lett. **110**, 186807 (2013).

[4] S. V. Eremeev, V. N. Men'shov, V. V. Tugushev, P. M. Echenique, and E. V. Chulkov, Phys. Rev. B **88**, 144430 (2013).

[5] V. Men'shov, V. Tugushev, S. Eremeev, P. M. Echenique, and E. Chulkov, Phys. Rev. B **88**, 224401 (2013).

[6] W. M. Yang *et al.*, Appl. Phys. Lett. **105**, 092411 (2014).

[7] T. Shoman, A. Takayama, T. Sato, S. Souma, T. Takahashi, T. Oguchi, K. Segawa, and Y. Ando, Nat. Commun. **6**, 6547 (2015).

[8] M. Li *et al.*, Phys. Rev. Lett. **115**, 087201 (2015).
[9] F. Katmis *et al.*, Nature (London) **533**, 513 (2016).
[10] Q. L. He *et al.*, Nat. Mater. **16**, 94 (2017).
[11] S. Rex, F. S. Nogueira, and A. Sudbo, Phys. Rev. B **94**, 020404 (2016).
[12] F. Hajiheidari, W. Zhang, and R. Mazzarello, Phys. Rev. B **94**, 125421 (2016).
[13] Z. L. Jiang, C. Z. Chang, C. Tang, P. Wei, J. S. Moodera, and J. Shi, Nano Lett. **15**, 5835 (2015).
[14] A. V. Matetskiy, I. A. Kibirev, T. Hirahara, S. Hasegawa, A. V. Zotov, and A. A. Saranin, Appl. Phys. Lett. **107**, 091604 (2015).
[15] L. A. Wray, Nat. Phys. **8**, 705 (2012).
[16] M. Z. Hasan and C. L. Kane, Rev. Mod. Phys. **82**, 3045 (2010).
[17] M. Gotte, M. Joppe, and T. Dahm, Sci. Rep. **6**, 36070 (2016).
[18] C. Z. Chang and M. D. Li, J. Phys.: Condens. Mat. **28**, 123002 (2016).
[19] C. X. Liu, S. C. Zhang, and X. L. Qi, Annu. Rev. Condens. Matter Phys. **7**, 301 (2016).
[20] C. Z. Chang *et al.*, Science **340**, 167 (2013).
[21] R. Yu, W. Zhang, H. J. Zhang, S. C. Zhang, X. Dai, and Z. Fang, Science **329**, 61 (2010).
[22] X. F. Kou *et al.*, Phys. Rev. Lett. **113**, 137201 (2014).
[23] J. G. Checkelsky, R. Yoshimi, A. Tsukazaki, K. S. Takahashi, Y. Kozuka, J. Falson, M. Kawasaki, and Y. Tokura, Nat. Phys. **10**, 731 (2014).
[24] X. Liu, H.-C. Hsu, and C.-X. Liu, Phys. Rev. Lett. **111**, 086802 (2013).
[25] Y. S. Hor *et al.*, Phys. Rev. B **81**, 195203 (2010).
[26] Y. L. Chen *et al.*, Science **329**, 659 (2010).
[27] C.-Z. Chang *et al.*, Nat. Mater. **14**, 473 (2015).
[28] M. D. Li, C. Z. Chang, L. J. Wu, J. Tao, W. W. Zhao, M. H. W. Chan, J. S. Moodera, J. Li, and Y. M. Zhu, Phys. Rev. Lett. **114**, 146802 (2015).
[29] W. Wang, C.-Z. Chang, J. S. Moodera, and W. Wu, NPG Quantum Mater. **1**, 16023 (2016).
[30] J. Zhang *et al.*, Science **339**, 1582 (2013).
[31] M. D. Li, W. P. Cui, J. Yu, Z. Y. Dai, Z. Wang, F. Katmis, W. L. Guo, and J. Moodera, Phys. Rev. B **91**, 014427 (2015).
[32] Y. Zhu, *Modern Techniques for Characterizing Magnetic Materials* (Kluwer Academic, Boston, 2005).
[33] See Supplemental Material at http://link.aps.org/supplemental/10.1103/PhysRevB.96.201301 for the image of the experimental setup, XRD, interpretation of spin asymmetry, fitting scheme, and fixed-SLD fitting.
[34] J. S. Zhang *et al.*, Nat. Commun. **2**, 574 (2011).
[35] Y. P. Jiang *et al.*, Phys. Rev. Lett. **108**, 016401 (2012).
[36] M. Bjorck and G. Andersson, J. Appl. Crystallogr. **40**, 1174 (2007).
[37] K. V. Price, R. M. Storn, and J. A. Lampinen, *Differential Evolution: A Practical Approach to Global Optimization*, Natural Computing Series (Springer, Berlin, 2005).
[38] H. W. Jang *et al.*, Phys. Rev. Lett. **104**, 197601 (2010).
[39] P. A. Kienzle, J. Krycka, N. Patel, and I. Sahin, *Refl1D package* (University of Maryland, College Park, MD, 2011).
[40] L. H. Bao *et al.*, Sci. Rep. **2**, 726 (2012).
[41] H. T. He, G. Wang, T. Zhang, I. K. Sou, G. K. L. Wong, J. N. Wang, H. Z. Lu, S. Q. Shen, and F. C. Zhang, Phys. Rev. Lett. **106**, 166805 (2011).
[42] J. Chen *et al.*, Phys. Rev. Lett. **105**, 176602 (2010).
[43] R. S. Popović, *Hall Effect Devices*, 2nd ed., Series in Sensors (Institute of Physics, Bristol, UK, 2004).
[44] D. Kim, S. Cho, N. P. Butch, P. Syers, K. Kirshenbaum, S. Adam, J. Paglione, and M. S. Fuhrer, Nat. Phys. **8**, 459 (2012).
[45] N. P. Butch, K. Kirshenbaum, P. Syers, A. B. Sushkov, G. S. Jenkins, H. D. Drew, and J. Paglione, Phys. Rev. B **81**, 241301 (2010).
[46] W. Luo and X.-L. Qi, Phys. Rev. B **87**, 085431 (2013).
[47] Y. G. Semenov, X. P. Duan, and K. W. Kim, Phys. Rev. B **89**, 201405 (2014).
[48] A. R. Mellnik *et al.*, Nature (London) **511**, 449 (2014).
[49] F. Mahfouzi, N. Nagaosa, and B. K. Nikolic, Phys. Rev. Lett. **109**, 166602 (2012).